Received: 10 September 2019 | Revised: 5 January 2020 | Accepted: 7 January 2020

DOI: 10.1002/mrm.28186

FULL PAPER

Magnetic Resonance in Medicine

# Multiphoton magnetic resonance in imaging: A classical description and implementation

**Victor Han**[1] | **Chunlei Liu**[1,2]

[1]Department of Electrical Engineering and Computer Sciences, University of California, Berkeley, Berkeley, California, USA

[2]Helen Wills Neuroscience Institute, University of California, Berkeley, Berkeley, California, USA

**Correspondence**
Chunlei Liu, Department of Electrical Engineering and Computer Sciences, University of California, Berkeley, 505 Cory Hall, MC #1770, Berkeley, CA 94720.
Email: chunlei.liu@berkeley.edu

**Funding information**
UC Berkeley

**Purpose:** To develop a classical geometric interpretation of multiphoton excitation and apply it to MRI. To investigate ways in which multiphoton excitation can enable novel imaging techniques.

**Theory and Methods:** We present a fully geometric view of multiphoton excitation by taking a particular rotating frame transformation. In this rotating frame, we find that multiphoton excitations appear just like single-photon excitations again, and therefore, we can readily generalize concepts already explored in standard single-photon excitation. With a homebuilt low frequency coil, we execute a standard slice selective pulse sequence with all of its excitations replaced by their equivalent two-photon versions. In the case of no extra hardware, we use oscillating gradients as a source of extra photons for excitation. Finally, with the multiphoton interpretation of oscillating gradients, we present a novel way to transform a standard slice selective adiabatic inversion pulse into a multiband version without modifying the RF pulse itself. The addition of oscillating gradients creates multiphoton resonances at multiple spatial locations and allows for adiabatic inversions at each location.

**Results:** With Bloch-Siegert shift corrections, analytical multiphoton excitation expressions match with Bloch equation simulations. Two-photon gradient-echo images of a lemon and a pork rib match with their single-photon counterparts. Frequency-offset RF combined with oscillating gradients generate excitation where the RF alone does not.

**Conclusion:** The multiphoton interpretation presents new flexibilities for imaging. Excitation needs not be bound to the Larmor frequency, which opens doors to RF pulse design beyond the usual filter design and the potential for further imaging innovations.

**KEYWORDS**

adiabatic, Bloch-Siegert shift, multiband, multiphoton, selective excitation, two-photon

  

# 1 | INTRODUCTION

Today's MRI assumes single-photon excitation.[1] That is, for each nuclear spin, a single photon accompanies the transition between energy states. This photon must resonate near the Larmor frequency. Here, we show that, instead of the usual single-photon resonance, we can excite multiphoton resonances to generate signal for MRI by using multiple magnetic field frequencies, none of which is near the Larmor frequency. Only the total energy absorbed by a spin must correspond to the Larmor frequency. One frequency must still be relatively close to the Larmor frequency, however, to avoid excessive RF field strengths and allow for practical imaging. Although virtual photons instead of real photons usually contribute more to signal,[2] we will use terms absorption and emission in this paper.

Multiphoton excitation has been described for NMR[3-8] and EPR.[9,10] For NMR, two-photon excitation has been used to permit simultaneous RF transmit and receive, as the transmitted RF has distinctive frequency from received RF tuned at the Larmor frequency. For continuous-wave EPR, $B_0$ modulation has been recast into a multiphoton excitation framework, where multiple photons polarized in the z-direction parallel to $B_0$ generate excitation together with a single photon polarized in the xy-plane. For MRI, however, multiphoton excitation has not yet been well explored. The idea that oscillating z-direction magnetic fields creates frequency "sidebands" is well known and has been used occasionally, both in excitation[11] and reception.[12] For excitation, it was used for simultaneous transmit and receive, and for reception, it was used to accelerate spatial information acquisition by increasing the receive bandwidth. However, as we will show, a multiphoton framework using Bloch equations and rotating frame transformations makes it clear that these multiphoton excitations excite extra resonances that look just like single-photon resonances, and concepts such as the Bloch-Siegert (BS) shift, slice selective excitation, and adiabatic RF pulses readily generalize.

Although we describe an effect that is quantum mechanical in name and in nature, the entirety of the analysis in this paper will be in a classical framework. We provide a completely geometrical interpretation of multiphoton effects. We show that with an extra RF coil, the standard slice-selective pulse sequence can be realized with all standard excitations replaced by multiphoton excitations. In the case of no extra hardware, extra photons can be provided by oscillating the gradient fields. In the case of oscillating gradients, the multiphoton interpretation leads to novel excitation pulse design techniques, a simple example of which is a multiband multiphoton adiabatic inversion pulse using only a standard hyperbolic secant adiabatic pulse[13] on the RF side. Such a pulse may be useful for simultaneous multislice imaging techniques.[14,15]

# 2 | THEORY

Standard single-photon excitation occurs when the RF field ($B_1$) is polarized in the xy-plane, perpendicular to the main magnetic field $B_0$. A variant of multiphoton effects occurs when we add more RF fields along the z-axis, parallel to the main magnetic field $B_0$. The term RF is used very loosely to include any oscillation frequency. Although it is also possible to have multiphoton effects with RF only in the xy-plane,[6] the effects for our pulse durations were not practical for generating reasonable flip angles and for avoiding overlap with single-photon excitation, so we will not consider them here.

## 2.1 | Two-photon excitation

### 2.1.1 | Phase-modulated rotating frame

Consider two $B_1$ fields with frequencies $\omega_{xy}$ and $\omega_z$ along the xy-plane and z-axis respectively. The total magnetic field in the laboratory frame is

$$B_z = B_0 + B_{1,z}\cos(\omega_z t), \tag{1}$$

$$B_x = B_{1,xy}\cos(\omega_{xy} t), \tag{2}$$

$$B_y = -B_{1,xy}\sin(\omega_{xy} t), \tag{3}$$

where the RF field in the xy-plane is clockwise circularly polarized; $B_{1,xy}$ and $B_{1,z}$ are amplitudes of each RF field. In a clockwise rotating frame with an angular velocity of $\omega_{rot}$, the effective $B_z$ field is

$$B_{z,eff} = B_z - \frac{\omega_{rot}}{\gamma}. \tag{4}$$

To generate time-invariant $B_{z,eff}$, we choose

$$\omega_{rot} = \omega_{xy} + \gamma B_{1,z}\cos(\omega_z t). \tag{5}$$

We refer this rotating frame as the phase-modulated rotating frame following.[3] This choice of $\omega_{rot}$ results in a non-stationary xy-plane RF field. To illustrate this effect, we examine the phase accrual of the xy-RF field in the rotating frame. Let $\theta$ be the phase, then

$$B_{x,eff} = B_{1,xy}\cos(\theta), \tag{6}$$

$$B_{y,eff} = B_{1,xy}\sin(\theta). \tag{7}$$

By definition,

$$\theta = \int_0^t (\omega_{rot} - \omega_{xy})dt = \frac{\gamma B_{1,z}}{\omega_z}\sin(\omega_z t). \tag{8}$$

Combining Equations 4-8 gives

$$B_{z,eff} = B_0 - \frac{\omega_{xy}}{\gamma}, \tag{9}$$

$$B_{x,eff} = B_{1,xy}\cos\left(\frac{\gamma B_{1,z}}{\omega_z}\sin(\omega_z t)\right), \tag{10}$$

$$B_{y,eff} = B_{1,xy}\sin\left(\frac{\gamma B_{1,z}}{\omega_z}\sin(\omega_z t)\right). \tag{11}$$

### 2.1.2 | Resonance conditions

Equations 10 and 11 can be Taylor expanded if $\frac{\gamma B_{1,z}}{\omega_z} \ll 1$ as

$$B_{x,eff} \approx B_{1,xy}, \tag{12}$$

$$B_{y,eff} \approx B_{1,xy}\frac{\gamma B_{1,z}}{\omega_z}\sin(\omega_z t). \tag{13}$$

From Equations 9, 12, and 13, three potential resonances exist depending on the relative values of the frequencies (Figure 1):

- Single-photon resonance: if $\omega_{xy} = \gamma B_0$, then $B_{z,eff} = 0$ and $B_{x,eff}$ tilts magnetization from the z-axis. This is the normal on-resonance condition.
- Two-photon resonances: if $\omega_{xy} = \gamma B_0 \pm \omega_z$, then $B_{z,eff} = \mp\omega_z/\gamma$. The linearly polarized RF field $B_{y,eff}$ oscillates with an angular frequency of $\omega_z$, matching the amplitude of $B_{z,eff}$, which induces resonances. These two new resonances correspond to state transitions where a single xy-polarized photon is absorbed and a single z-polarized photon is absorbed or emitted, depending on whether the xy-frequency is below or above the Larmor frequency. From Equation 13, just like with single photon excitation, by taking another rotating frame with angular velocity $\mp\omega_z$ and dividing the $B_{y,eff}$ amplitude by two for only one circularly polarized component, in agreement with prior work, the effective angular nutation frequency for two-photon excitation is

$$\omega_{nut} = \frac{\gamma B_{1,xy}\gamma B_{1,z}}{2\omega_z}. \tag{14}$$

Until this point, we have essentially followed the classical approach of Eles and Michal[5] with two differences: arbitrary frequencies and separated $B_{1,xy}$ and $B_{1,z}$ fields.

## 2.2 | Multiphoton excitation

If more terms are kept in the Taylor expansion of Equations 10 and 11, we can analyze higher-order excitations with three or more photons. However, Taylor expansion

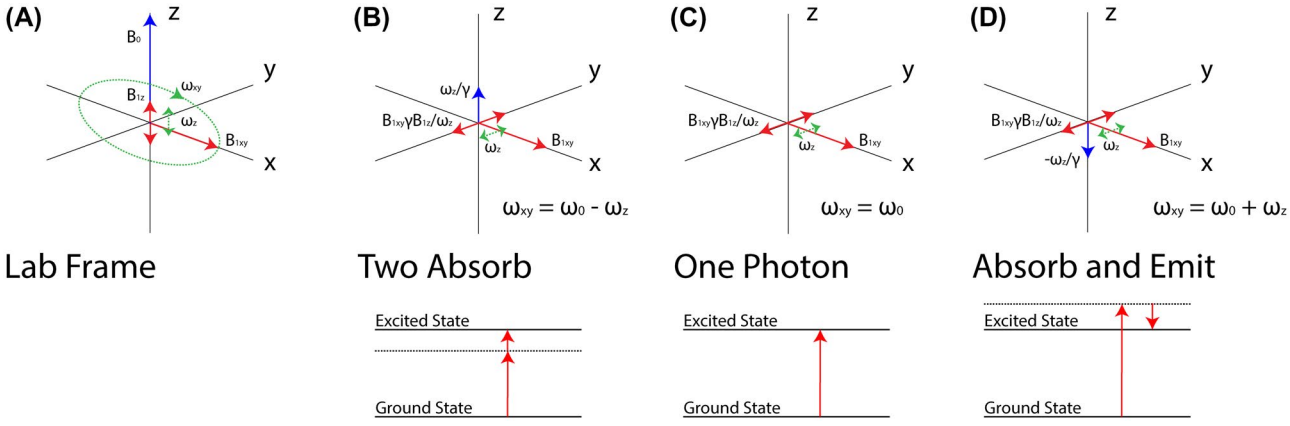


**FIGURE 1** Single- and two-photon excitation conditions. (A) Magnetic field setup in the laboratory frame with arbitrary frequencies for the xy- and z-RF fields. (B) In the phase-modulated rotating frame with $\omega_{xy} = \gamma B_0 - \omega_z$, there is a remaining static z-field that resonates with the oscillating field on the y-axis. In this case, both a xy- and z-photon are absorbed. (C) In the phase-modulated rotating frame with $\omega_{xy} = \gamma B_0$, there is no remaining static z-field, and the static x-field causes the resonance. This is the standard single-photon resonance. (D) In the phase-modulated rotating frame with $\omega_{xy} = \gamma B_0 + \omega_z$, there is a remaining static z-field that resonates with the oscillating field on the y-axis. In this case, a xy-photon is absorbed while a z-photon is emitted

requires $\frac{\gamma B_{1,z}}{\omega_z} \ll 1$. Alternatively, we can exactly expand $B_{x,eff}$ and $B_{y,eff}$ using Bessel functions (Appendix), which reveals that for any integer $n$, resonance occurs whenever

$$\omega_{xy} = \gamma B_0 + n\omega_z, \tag{15}$$

and for each integer $n$, the corresponding effective angular nutation frequency is

$$\omega_{nut} = \gamma B_{1,xy} J_n\left(\frac{\gamma B_{1,z}}{\omega_z}\right). \tag{16}$$

$J_n$ represents the Bessel function of the first kind of order $n$. $n$ represents the number of z-axis photons in the resonance. As the maximum of Bessel functions occurs at gradually larger arguments for higher orders, larger $\frac{\gamma B_{1,z}}{\omega_z}$ is needed to generate multiphoton resonances. Generalizing further, if we have photons of different frequencies along the z-axis, we simply multiply another Bessel function for that frequency (Appendix). In the case of two different frequencies, we have resonances whenever

$$\omega_{xy} = \gamma B_0 + n\omega_{z1} + m\omega_{z2}, \tag{17}$$

and for each $n$ and $m$, the corresponding angular nutation frequency is given by

$$\omega_{nut} = \gamma B_{1,xy} J_n\left(\frac{\gamma B_{1,z1}}{\omega_{z1}}\right) J_m\left(\frac{\gamma B_{1,z2}}{\omega_{z2}}\right). \tag{18}$$

As a side note, Bessel function expansion has also been used in the context of excitation k-space with sinusoidal gradient waveforms.[16,17]

## 2.3 | Bloch-Siegert shift

Off-resonance RF fields slightly shift resonance frequencies, a phenomenon termed the Bloch-Siegert (BS) shift.[18,19] This shift also affects multiphoton excitation, as off-resonant RF fields are always used. The resulting BS shifts can be calculated based on all the off-resonant terms in the phase-modulated rotating frame. Specifically, each off-resonant term adds a BS shift. To the second order, the BS shift is

$$\omega_{BS} = \frac{\left(\gamma B_{1,off}\right)^2}{2\omega_{off}}, \tag{19}$$

where $B_{1,off}$ is the magnitude of the off-resonant RF field and $\omega_{off}$ is the frequency offset from the resonance, which can be a single-photon resonance or any multiphoton resonance. In theory, the number of off-resonant terms, whose amplitudes are given by the integer orders of the Bessel function, will be infinite. The infinite sums can be approximated by the Carson's bandwidth rule,[20] which heuristically states that ~98% of the power of a frequency-modulated signal will be contained in a bandwidth of $2(\beta+1)B$, where $\beta$ is the peak modulation index and $B$ is the highest frequency in the modulating signal. In our case, $\beta$ is the largest $\frac{\gamma B_{1,zn}}{\omega_{zn}}$ and $B$ is the largest $\omega_{zn}$.

Consider a case with one $B_{1,xy}$ and two $B_{1,z}$, where resonances occur at $\omega_{xy} = \gamma B_0 + k\omega_{z1} + l\omega_{z2}$. Then, the off-resonant terms in the phase-modulated rotating frame are (Appendix, Equation A15)

$$B_{xy,off} = B_{1,xy} \sum_{(n,m)\neq(k,l)} J_n\left(\frac{\gamma B_{1,z1}}{\omega_{z1}}\right) J_m\left(\frac{\gamma B_{1,z2}}{\omega_{z2}}\right) e^{i\left((n-k)\omega_{z1}+(m-l)\omega_{z2}\right)}. \tag{20}$$

Each of these terms contributes to the BS shift as approximated by Equation 19, resulting in a total BS shift of

$$\omega_{BS\,total} = \frac{\left(\gamma B_{1,xy}\right)^2}{2} \sum_{(n,m)\neq(k,l)} \frac{\left(J_n\left(\frac{\gamma B_{1,z1}}{\omega_{z1}}\right) J_m\left(\frac{\gamma B_{1,z2}}{\omega_{z2}}\right)\right)^2}{(n-k)\,\omega_{z1} + (m-l)\,\omega_{z2}}. \tag{21}$$

The summation can be evaluated numerically with Carson's bandwidth rule.

# 3 | METHODS

## 3.1 | Numerical simulation

Bloch simulations were performed in MATLAB R2017a (The MathWorks, Natick, MA) using the built-in ode45 or ode113 solver. All xy-frequencies represent offsets from the Larmor frequency, as we used the rotating frame at the Larmor frequency.

### 3.1.1 | Resonance verification

First, multiphoton resonances were verified by evaluating resulting transverse magnetization versus various combinations of xy- and z-RF frequencies (10-ms hard pulses). RF in xy and z were swept from −30 kHz to 30 kHz and from 0 to 30 kHz with a step size of 60 and 30 Hz, respectively. For each simulated point, $B_{1,z}$ was chosen such that $\frac{\gamma B_{1,z}}{\omega_z} = 1$. $B_{1,xy}$ was kept at a constant $1\mu T$.

### 3.1.2 | Nutation frequency verification

Simulation was then compared with the analytical nutation frequency expressions over a wide range of magnetic

field strengths and frequencies that may be encountered in practice. Because the analytical expressions give resonance nutation frequencies, simulation must consider the BS shift as described in the theory section. For example, if a two-photon resonance is desired with $\omega_{xy} = \omega_0 + 10{,}000$ rad/s and $\omega_z = 10{,}000$ rad/s, and it was predicted that the BS shift was +87 rad/s for this resonance, then the xy-frequency was shifted by the BS shift such that we still hit the desired resonance. That is, for the simulation, the frequencies $\omega_{xy} = \omega_0 + 10{,}087$ and $\omega_z = 10{,}000$ would be used instead. Analytic transverse magnetizations were calculated using an effective flip angle obtained by multiplying the effective nutation frequency with the hard pulse duration of 10 ms.

## 3.2 | Scanner experiments

All MRI experiments except for the multiband RF pulses were performed on an Aspect 1T wrist scanner (Aspect Imaging, Shoham, Isreal). The multiband RF experiments were performed on a GE 3T MR750w scanner (Waukesha, WI).

### 3.2.1 | Experiment I: two-photon excitation with an extra z-RF coil

Two-photon RF pulses were transmitted simultaneously with a commercial coil at 44.73 MHz (i.e., Larmor frequency plus 130 kHz) and a homebuilt solenoid coil at 130 kHz (Figure 2) in the same manner as shown in Figure 5 of Eles and Michal.[5] The homebuilt coil, resonated and matched at 130 kHz, was inserted into the commercial coil, producing RF in the $B_0$ direction. The input to the 130-kHz coil was connected to a custom-built power amplifier (100 W, operational between 100 kHz to 1 MHz), which was connected to an arbitrary waveform generator (Keysight 33600A; gated burst mode and 130 kHz). The gating signal was synchronized to the scanner's control signal for the transmit/receive-switch, such that the 130 kHz signal was generated whenever the scanner transmitted a RF pulse. The 130 kHz shift was chosen as the shift is sufficiently large to avoid single-photon resonances. That is, all the frequencies transmitted by the two coils were outside of the range of single-photon excitation within the field of view. Gradient-echo images of a lemon were acquired with: TR/TE = 500/3.0 ms, FA = 10°, 500-μs sincgauss pulse, resolution = 0.625 × 0.625 × 3 mm$^3$, 80 × 80 mm$^2$ FOV, 10 slices, 40-kHz readout bandwidth, axial orientation, 66-s scan time. Gradient-echo images of a country-style pork rib were acquired with: TR/TE = 500/8.4 ms, FA = 45°, 10-ms sincgauss pulse, resolution = 0.625 × 0.625 × 2 mm$^3$, 80 × 80 mm$^2$ FOV, 10 slices, 40-kHz readout bandwidth, coronal orientation, 66-s scan time.

### 3.2.2 | Experiment 2: two-photon excitation with gradient coils

Oscillating gradients can also provide z-axis RF. For example, given a sinusoidal gradient vector $\vec{\mathbf{G}}\sin(\omega_z t)$, the amplitude of the resulting z-axis RF is spatially linearly varying as

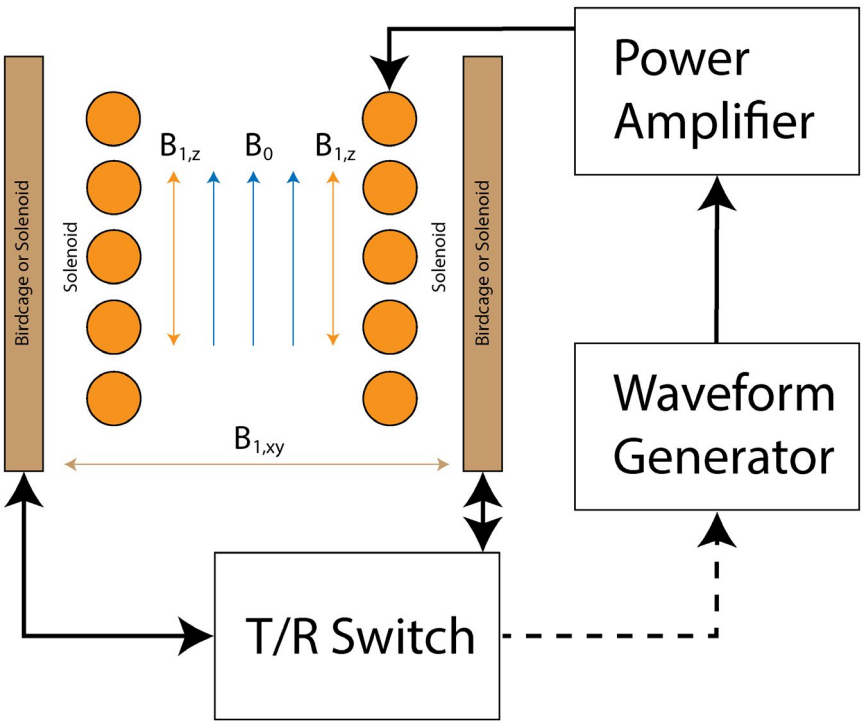


**FIGURE 2** Example two-photon scanning setup. An extra $B_{1,z}$ solenoid is aligned with $B_0$. The control signal for the transmit/receive-switch (T/R switch) from the scanner triggers output from the waveform generator. The triggered 130 kHz signal is amplified and fed into the $B_{1,z}$ coil

$$B_{1,z} = \vec{\mathbf{G}} \cdot \vec{\mathbf{r}} \sin(\omega_z t). \quad (22)$$

The corresponding flip angles are therefore also spatially varying following the nutation frequency in Equation 16. As an illustration, a copper-sulfate-solution phantom was non-selectively excited using the x or y gradient oscillating at 16 kHz in conjunction with an xy-RF offset by −16 kHz from the Larmor frequency. A Larmor-frequency 180° pulse was used to only refocus the center slice. Other parameters are: TR/TE = 500/8.4 ms, 700-μs excitation pulse (180° SLR RF pulse and 0.386 G/cm sinusoidal gradient), 700-μs 180° SLR refocusing pulse, resolution = 0.625 × 0.625 × 5 $mm^3$, 80 × 80 $mm^2$ FOV, 2 slices, 40-kHz readout bandwidth, axial orientation, 66-s scan time.

#### 3.2.3 | Experiment 3: multiband multiphoton adiabatic pulse

Using gradients for multiphoton excitation opens an avenue for novel pulse designs. As an example, we created a multiband multiphoton adiabatic inversion pulse by combining a standard hyperbolic secant adiabatic inversion pulse with an oscillating gradient, in contrast to previous approaches that add multiple pulses together[21] or periodically switch RF on and off.[22] To implement it on the GE scanner, a fast spin echo pulse sequence with an inversion recovery module using a multiband hyperbolic secant inversion pulse was programmed in KSFoundation EPIC.[23] To view the multiband inversion profiles, the inversion-pulse gradients were applied along an axis perpendicular to the fast spin echo imaging plane. A plot of the pulse waveforms is shown in Supporting Information Figure S1.

With a spherical phantom, we compared several combinations of RF and gradient waveforms with an inversion recovery time of 0.5 s. First, we used an 8-ms hyperbolic secant RF pulse with parameters $A_0 = 22$ μT, μ = 4.9, and β = 800 rad/s. Adding a constant slice-selective 0.2 G/cm DC gradient results in a single inversion band. Superimposing a 3-kHz AC gradient with an amplitude equal to 1.5 times that of the DC gradient produces multiband inversion. This combination ensures that at the spatial locations where the local Larmor frequency is offset by 3 kHz from the center, $\frac{\gamma B_{1,z}}{\omega_z} = 1.5$, and the two-photon resonance is the most efficient resonance compared to any other resonance (Supporting Information Table S1). Similarly, at spatial locations with local Larmor frequencies offset by 6 kHz, we have $\frac{\gamma B_{1,z}}{\omega_z} = 3.0$ and the three-photon resonance is the most efficient resonance. Therefore, for a field of view encompassing 6-kHz offsets in either direction, we expect a five-band adiabatic pulse composed of single-, two-, and three-photon adiabatic inversions. Next, a 12-ms RF pulse (μ = 4 and β = 600 rad/s) and a 0.2 G/cm DC gradient superimposed with a 5.5-kHz AC gradient were used to produce three thinner bands. Finally, to demonstrate unevenly spaced bands, the 12-ms pulse was applied with a 0.175 G/cm DC gradient that was superimposed with a 5.5-kHz and a 4-kHz AC gradient with amplitudes of 0.2625 and 0.175 G/cm, respectively. These values were chosen such that higher-order bands were not formed in the field of view because of negligible excitation efficiency.

Under procedures approved by our institution's IRB, a healthy volunteer was scanned. For the human brain, the 5 bands produced by 8-ms multiphoton adiabatic inversion pulses as in the first phantom experiment were imaged with inversion recovery times of 400 ms, 650 ms, and 2500 ms. The parameters of the fast spin echo readout were: ETL = 8, TR/TE = 4000/44 ms, FA = 90°, FOV = 230 × 230 $mm^2$, matrix = 256 × 256, 1 slice of 2-mm thickness, 62.5-kHz readout bandwidth, axial orientation, 128-s scan time.

## 4 | RESULTS

### 4.1 | Numerical simulation

#### 4.1.1 | Resonance verification

The transverse magnetization generated by two perpendicular $B_1$ pulses ($B_{1,xy}$ and $B_{1,z}$) showed five lines of elevated intensity versus the 2D frequency sweep (Figure 3A). The center brightest line, corresponding to $\Delta\omega_{xy} = 0$, represents the single-photon resonance. The two lines closest to the center line represent the two-photon resonances, where $\Delta\omega_{xy} \approx \pm\omega_z$. The two furthest lines represent the three-photon resonances, where $\Delta\omega_{xy} \approx \pm 2\omega_z$. Note that with the fixed ratio of $\frac{\gamma B_{1,z}}{\omega_z} = 1$, the excitation efficiency decreases toward higher-order resonances. To further illustrate the multiphoton-resonance nature, Figure 3B,C show representative time and frequency domain plots of a two-photon excitation. Note that there is no component of the excitation at the Larmor frequency. Visualization of magnetization nutation is shown in Supporting Information Videos S1-S7.

#### 4.1.2 | Nutation frequency verification

Without BS shift compensation, there was significant deviation between Bloch simulation and transverse magnetization derived analytically from Equation 16, especially at higher $B_{1,xy}$ strengths (Figure 4D-F). However, with the pre-compensation, the simulation matches nearly exactly the analytical expressions (Figure 4A-C). The effective flip angle increases linearly with the strength of $B_{1,xy}$ (Figure 4A) but changes nonlinearly with increasing $B_{1,z}$ and $\omega_z$, as $J_1\left(\frac{\gamma B_{1,z}}{\omega_z}\right)$

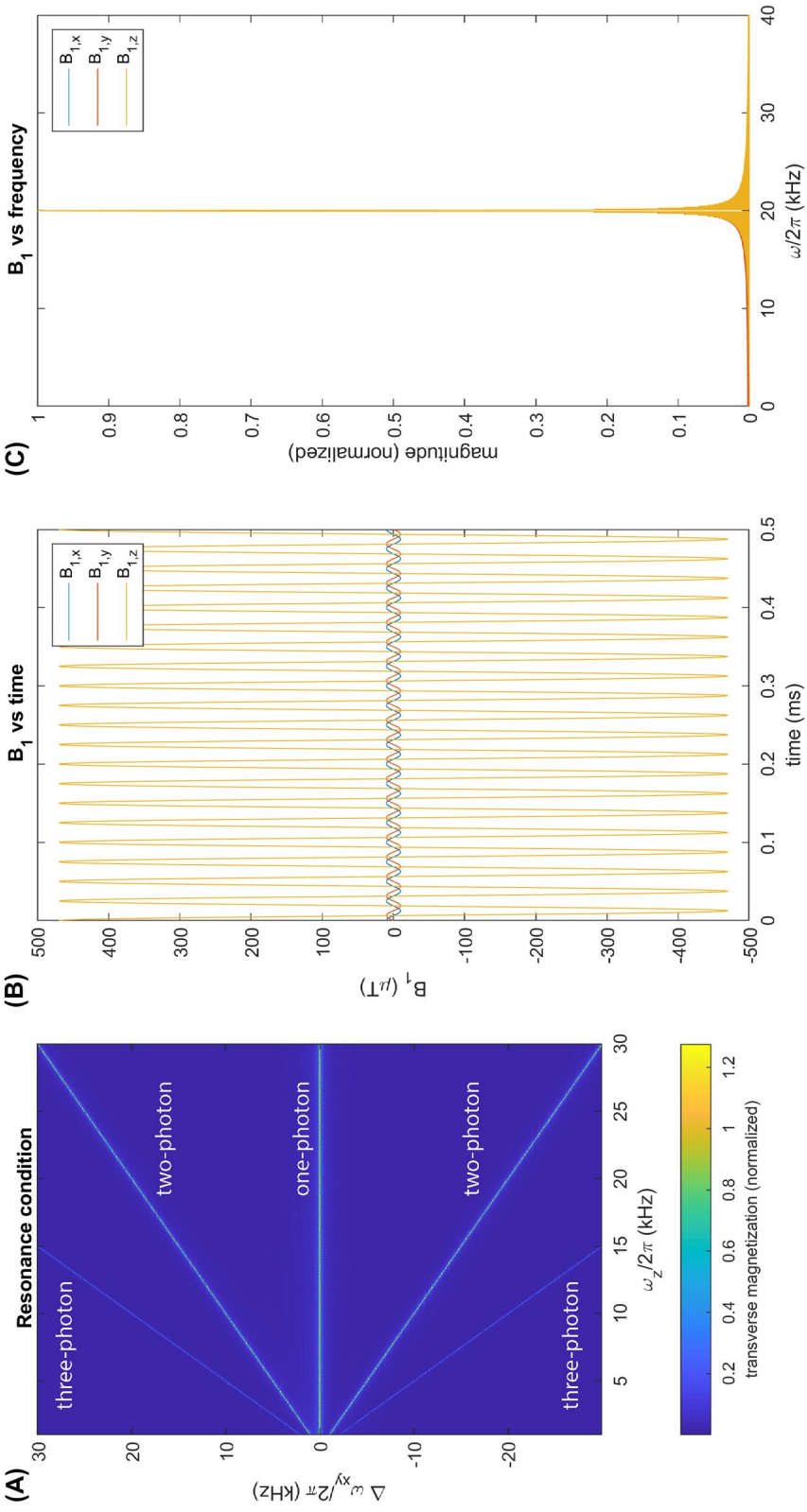


**FIGURE 3** Multiphoton resonance. (A) Transverse magnetization versus 2D frequency sweep. One, two, and three photon resonance lines can be seen. (B) Example time domain fields for the $B_1$ pulses generating a two-photon resonance and (C) the corresponding frequency-domain fields. The three curves overlap in (C)

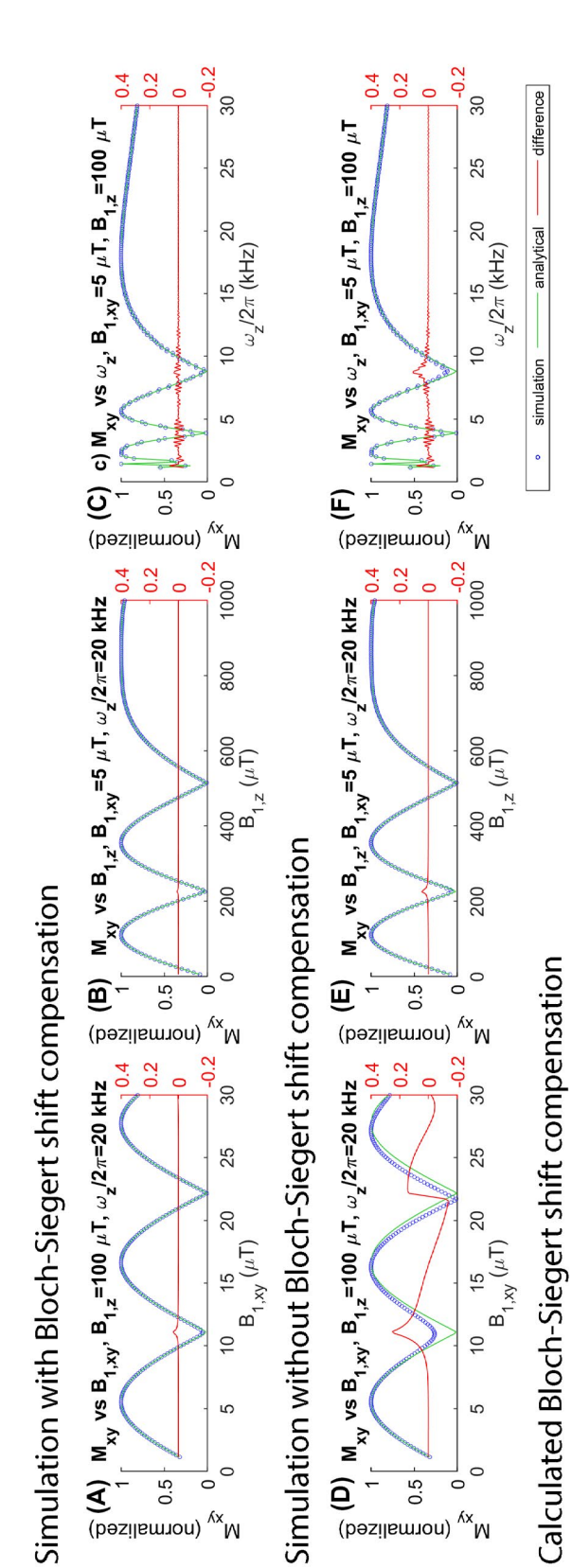


**FIGURE 4** BS shifts for two-photon excitation for various parameters. (A-C) Simulation and analytical transverse magnetization for various $B_{1,xy}$, $B_{1,z}$, and $\omega_z$, respectively. In simulation, $\omega_{xy}$ values are set to be equal to $\omega_z$ with slight adjustments by the BS shift as described in the text such that resonances are accurate. Differences between the simulated and analytical values are plotted in red with the axis on the right-hand side. (D-F) Same as (A)-(C), except that no BS shift pre-adjustments are made for the simulations. Note that the differences between simulation and analytical transverse magnetization are nearly an order of magnitude more than in (A)-(C) for these ranges of parameters. (G-I) BS shifts calculated and used for the pre-adjustments in (A)-(C) simulations

oscillates nonperiodically (Figure 4B,C). Potential deviations between simulation and analytical expressions may occur when the BS shift approximation is not accurate. The second-order BS shift approximation used here, however, works well for the range of values shown. Although the amplitude of $B_{1,xy}$ has the strongest effect, all parameters influence the BS shift.

## 4.2 | Scanner experiments

### 4.2.1 | Experiment I: two-photon excitation with an extra z-RF coil

With a standard gradient-echo sequence, the two-photon resonance produces similar image quality as those of the single-photon resonance for both the lemon and pork rib (Figure 5). Spatial shading (Figure 5B) is because of inhomogeneity of the $B_{1,z}$ coil and magnetic field deviations from the z-axis. SNR differences (Figure 5C,D) are because of different tunings of the receive-coil frequency and therefore matching with the low noise amplifier, because frequencies were tuned to $B_{1,xy}$ transmit frequencies on the transceiver coil. Any other slight SNR differences may be because of inaccurate flip angle calibration. As such, no quantitative SNR comparison is made.

### 4.2.2 | Experiment 2: two-photon excitation with gradient coils

When using gradients as a z-axis RF source, the frequency range is limited by the gradient slew rate, and the resulting RF field varies linearly in space (Equation 22). Different excitation patterns corresponding to different flip angles were generated with $G_x$ and $G_y$ gradients (Figure 6A-D). When the z-axis RF (i.e., oscillating $G_x$ and $G_y$) is turned off, no excitation occurs (Figure 6E), demonstrating its two-photon nature. This two-photon excitation differs from spatial and spectral selective excitation that assumes RF transmitted and received both at the Larmor frequency and makes a small-tip approximation.[17]

### 4.2.3 | Experiment 3: multiband multiphoton adiabatic pulse

Figure 7 shows the expected adiabatic inversion bands on a spherical phantom and human brain. It is possible to create more bands. However, as the Bessel function values become more dispersed with higher-order resonances, power efficiency for the higher-order multiphoton adiabatic inversions decrease and the total RF power needs to be increased to achieve full inversions for the higher-order resonances.

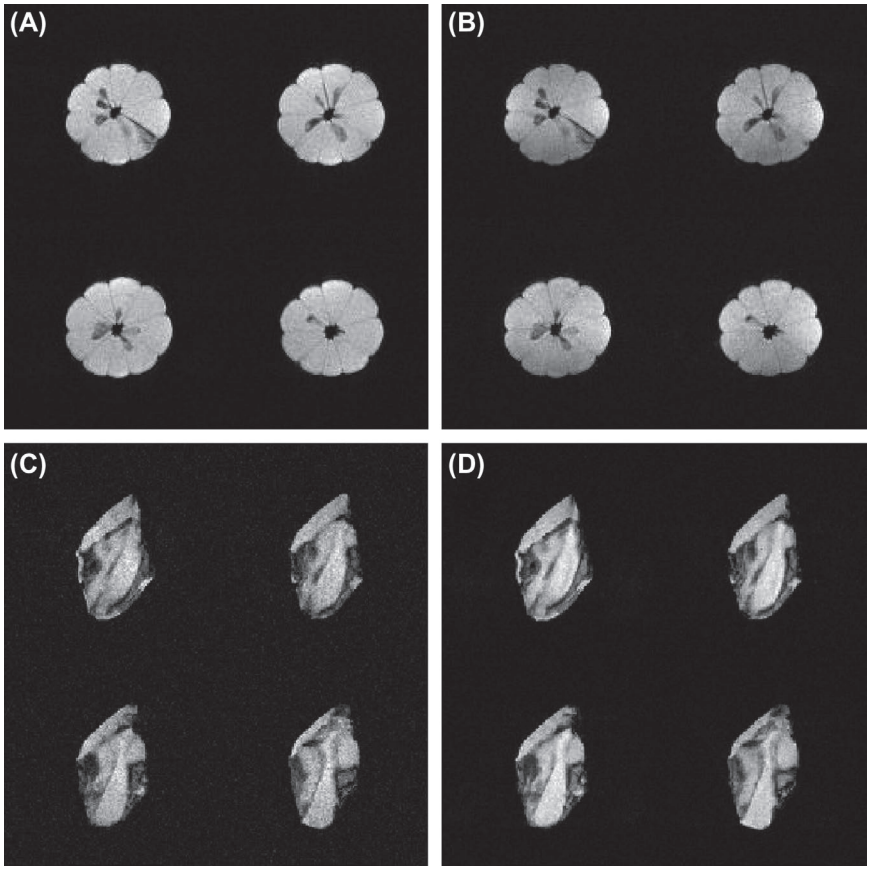


**FIGURE 5** Two-photon gradient-echo sequence. (A) Single-photon excitation for a lemon. (B) Two-photon excitation for the lemon. (C) Single-photon excitation for a country-style pork rib. (D) Two-photon excitation for the pork rib. In (B) and (D), all transmit xy-RF was shifted up by 130 kHz and a 130-kHz square wave z-RF was transmitted simultaneously with the xy-RF

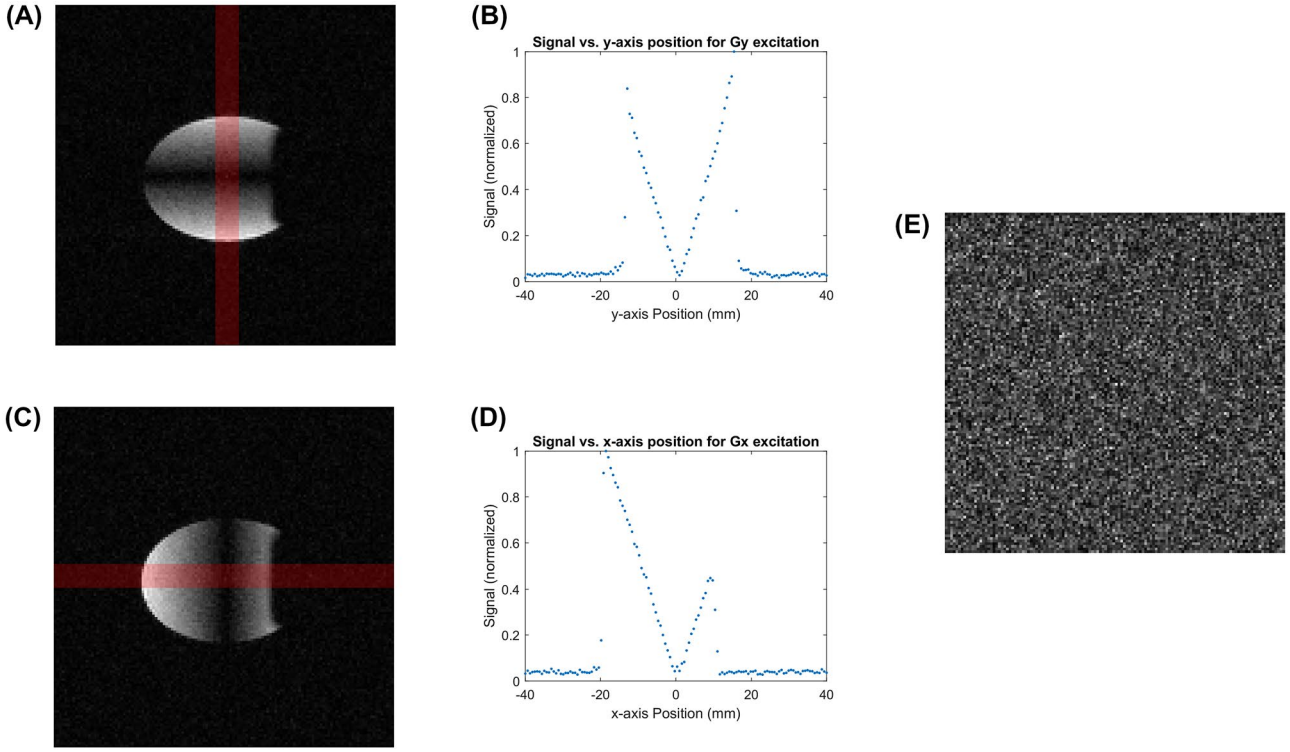


**FIGURE 6** Spin-echo with two-photon excitation. (A) Image acquired after excitation with RF offset by 16 kHz and $G_y$ gradient (up/down direction) oscillating at 16 kHz and (B) 1D line plot of signal versus y-axis position for a center band of the image showing linear intensity variations as predicted by theory for small $\frac{\gamma B_{1z}}{\omega_z}$ and flip angle. (C) Excitation with RF offset by 16 kHz and $G_x$ gradient (left/right direction) oscillating at 16 kHz and (D) 1D line plot of signal versus x-axis position for a center band of the image showing linear intensity variations. The red bands in (A) and (C) indicate the signal locations of (B) and (D), respectively. (E) Excitation with RF offset by 16 kHz and no gradients

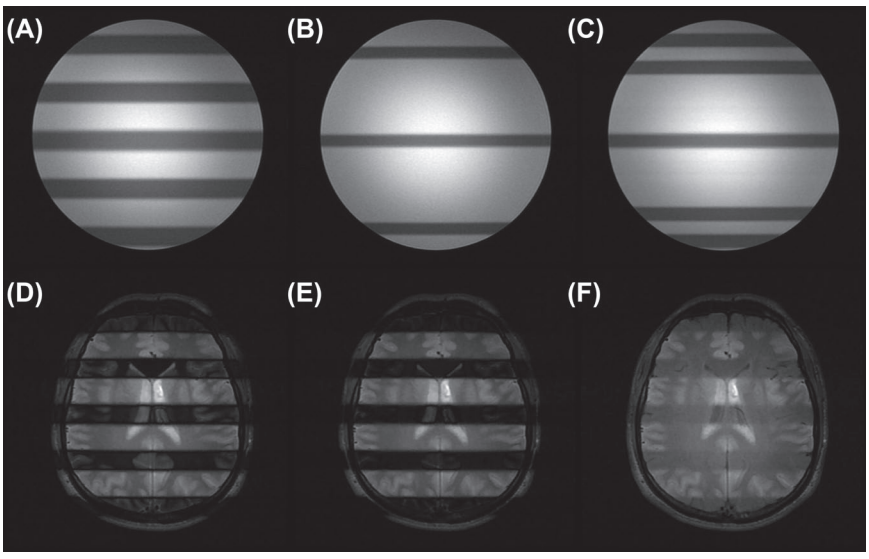


**FIGURE 7** Multiband multiphoton adiabatic inversion. Multiband adiabatic inversions on a spherical phantom and a human brain with various parameters. (A) An 8-ms hyperbolic secant RF pulse ($A_0 = 22$ μT, $\mu = 4.9$, $\beta = 800$ rad/s) with a 0.2 G/cm DC gradient and a 0.3 G/cm 3-kHz AC gradient. (B) A 12-ms RF pulse ($\mu = 4$, $\beta = 600$ rad/s) with a 0.2 G/cm DC gradient and a 0.3 G/cm 5.5-kHz AC gradient. (C) The same RF as in (B) with a 0.175 G/cm DC gradient superimposed with a 5.5-kHz and a 4-kHz AC gradient with amplitudes of 0.2625 G/cm and 0.175 G/cm, respectively. For the human brain, five-band multiphoton adiabatic inversion pulses as in (A) were imaged with inversion recovery times of (D) 400 ms, (E) 650 ms, and (F) 2500 ms. The white matter, gray matter, and CSF are seen to be selectively attenuated based on the inversion recovery time, respectively

Other frequencies in the rotating frame of the multiphoton resonance may also gain relative power and affect the success of the adiabatic pulse. Nevertheless, when producing multiple inversion bands, multiphoton resonances increase RF efficiency compared to the traditional method of adding independent pulses,[21] as the same RF pulse produces excitation in each band. In theory, to achieve at least the same effective pulse amplitude for the multiband resonances as that of an original single-band pulse for single-photon resonance, we would need to multiply the RF amplitude by the inverse of the minimum Bessel function multiplier. In the five-band case with up to three-photon resonances shown, this is $1/J_2(3.0) = 2.06$. By multiplying RF amplitude by 2.06, we can achieve four extra bands, and if more ripple is acceptable in some bands, RF amplitude potentially need not even be increased at all. In comparison to Koopmans et al,[22] this method may be slightly less power efficient because of the less than or equal to unity Bessel function factor, but it allows for much shorter pulses as the RF is not paused for gradients. Furthermore, the ability to make unevenly spaced pulses is potentially useful. 1D simulations of the inversion profiles for similar pulses are shown in Supporting Information Figure S2.

## 5 | DISCUSSION AND CONCLUSIONS

We present here a general approach for analyzing and implementing multiphoton MRI under a classical framework. The approach unifies single-photon and multiphoton excitation under the same mathematical framework. The approach is validated with both simulation and experiments.

The multiphoton interpretation predicts a type of excitation that occurs even when the RF field has no frequency components near the Larmor frequency. In this paper, we have provided a way to determine the effects of such excitations. With the multiphoton interpretation, true-resonance conditions are established, and with this knowledge, extensions for shaped pulses and nonlinear effects such as the BS shift and adiabatic pulses follow.

Because multiphoton excitation applies RF fields with frequencies significantly shifted from the Larmor frequency, one compelling application of multiphoton MRI is simultaneous transmit and receive via frequency isolation. Simultaneous transmit and receive MRI has been implemented in other ways,[24-27] and provides the advantage of high imaging efficiency without dead time and high SNR with minimal $T_2$ and $T_2^*$ decay, especially useful for imaging short-$T_2$ species. However, as Brunner et al[11] also noted for sideband excitation, such a scheme with multiphoton excitation may be most practical at low main magnetic field strengths. This is because the efficiency of multiphoton excitation depends on an absolute, not relative, offset from the Larmor frequency. A simultaneous transmit and receive scheme would require filters to separate the transmit frequency from the received frequency. Separating a 100 kHz and 50 kHz transmit and receive would be much easier than separating a 100.1 MHz and 100.05 MHz transmit and receive. Furthermore, at low fields, SAR from the decreased excitation efficiency is a smaller concern, and larger RF fields are easier to produce at lower frequencies.

Multiphoton MRI offers a new way to explore novel contrast for MRI. Although, post multiphoton excitation, the magnetization evolves similarly as in single-photon excitation, the multiphoton excitation pulses can alter signal evolution during excitation. For example, excitation RF is known to affect relaxation rates such as with $T_{1\rho}$ and the recently described relaxation along a fictitious field.[28] Multiphoton excitation provides a new way to manipulate multiple RF waveforms and sample various interaction time scales. For example, a $B_{1,\tilde{z}}$ field could be chosen to be in sync with biological or chemical processes of interest and impact the corresponding MRI signal. The choice of multiphoton excitation RF frequencies could also alter the effect of magnetization transfer and chemical-exchange saturation transfer.

Finally, multiphoton MRI offers extra degrees of freedom for designing excitation pulses. As already shown, a simple single-band adiabatic inversion pulse may be made multiband via a proper choice of gradient waveforms. In general, for slice-selective excitation, RF pulse design can be extended beyond the usual filter design. For more general 3D selective excitation, an image space multiphoton excitation framework could be used instead of excitation k-space.[29] Without a small flip angle approximation, but with some BS shift approximations, excitation at each spatial location for time varying RF and gradients may be calculated. As gradient[30,31] and traditional RF coils gain more channels and spatial–temporal flexibility, much more can be achieved using multiphoton MRI to encode spatial, spectral, and temporal information.

### ACKNOWLEDGMENTS

The authors thank Michael Lustig, PhD, of UC Berkeley for discussions and assistance with the Aspect scanner, Aspect Imaging for providing the wrist scanner, and Neelesh Ramachandran of UC Berkeley for assistance with hardware construction.

### ORCID

*Victor Han* https://orcid.org/0000-0003-3093-2549
*Chunlei Liu* https://orcid.org/0000-0001-8816-4832

### REFERENCES

1. Lauterbur PC. Image formation by induced local interactions: examples employing nuclear magnetic resonance. *Nature*. 1973; 242:190–191.

2. Hoult DI, Ginsberg NS. The quantum origins of the free induction decay signal and spin noise. *J Magn Reson*. 2001;148:182–199.
3. Michal CA. Nuclear magnetic resonance noise spectroscopy using two-photon excitation. *J Chem Phys*. 2003;118:3451–3454.
4. Eles PT, Michal CA. Two-photon two-color nuclear magnetic resonance. *J Chem Phys*. 2004;121:10167–10173.
5. Eles PT, Michal CA. Two-photon excitation in nuclear magnetic and quadrupole resonance. *Prog Nuclear Magn Reson Spectrosc*. 2010;56:232–246.
6. Zur Y, Levitt MH, Vega S. Multiphoton NMR spectroscopy on a spin system with $I = 1/2$. *J Chem Phys*. 1983;78:5293–5310.
7. Boscaino R, Messina G. Double quantum coherent transients in a two-level spin system: a vectorial model. *Physica B+C*. 1986;138:179–187.
8. Abragam A. *The principles of nuclear magnetism*. London: Clarendon Press; 1961:599.
9. Gromov I, Schweiger A. Multiphoton resonances in pulse EPR. *J Magn Reson*. 2000;146:110–121.
10. Saiko AP, Fedaruk R, Markevich SA. Multi-photon transitions and Rabi resonance in continuous wave EPR. *J Magn Reson*. 2015;259:47–55.
11. Brunner D, Pavan M, Dietrich B, Rothmund D, Heller A, Pruessmann K. Sideband excitation for concurrent RF transmission and reception. In Proceedings of the 19th Annual Meeting of ISMRM, Montreal, Canada, 2011. Abstract 0625.
12. Scheffler K, Loktyushin A, Bause J, Aghaeifar A, Steffen T, Schölkopf B. Spread-spectrum magnetic resonance imaging. *Magn Reson Med*. 2019;82:877–885.
13. Garwood M, DelaBarre L. The return of the frequency sweep: designing adiabatic pulses for contemporary NMR. *J Magn Reson*. 2001;153:155–177.
14. Larkman DJ, Hajnal JV, Herlihy AH, Coutts GA, Young IR, Ehnholm G. Use of multicoil arrays for separation of signal from multiple slices simultaneously excited. *J Magn Reson Imaging*. 2001;13:313–317.
15. Setsompop K, Gagoski BA, Polimeni JR, Witzel T, Wedeen VJ, Wald LL. Blipped-controlled aliasing in parallel imaging for simultaneous multislice echo planar imaging with reduced g-factor penalty. *Magn Reson Med*. 2012;67:1210–1224.
16. Powell NJ, Jang A, Park JY, Valette J, Garwood M, Marjańska M. Gradient rotating outer volume excitation (GROOVE): a novel method for single-shot two-dimensional outer volume suppression. *Magn Reson Med*. 2015;73:139–149.
17. Meyer CH, Pauly JM, Macovskiand A, Nishimura DG. Simultaneous spatial and spectral selective excitation. *Magn Reson Med*. 1990;15:287–304.
18. Bloch F, Siegert A. Magnetic resonance for nonrotating fields. *Phys Rev*. 1940;57:522–527.
19. Ramsey NF. Resonance transitions induced by perturbations at two or more different frequencies. *Phys Rev*. 1955;100:1191–1194.
20. Couch LW. *Digital & analog communication systems*, 8th ed. Upper Saddle River: Pearson; 2012:792.
21. Goelman G, Leigh JS. Multiband adiabatic inversion pulses. *J Magn Reson A*. 1993;101:136–146.
22. Koopmans PJ, Boyacioğlu R, Barth M, Norris DG. Simultaneous multislice inversion contrast imaging using power independent of the number of slices (PINS) and delays alternating with nutation for tailored excitation (DANTE) radio frequency pulses. *Magn Reson Med*. 2013;69:1670–1676.
23. Skare S, Avventi E, Norbeck O, Ryden H. An abstraction layer for simpler EPIC pulse programming on GE MR systems in a clinical environment. In Proceedings of the 25th Annual Meeting of ISMRM, Honolulu, United States, 2017. Abstract 3813.
24. Davies GR, Lurie DJ, Hutchison JMS, McCallum SJ, Nicholson I. Continuous-wave magnetic resonance imaging of short T2 materials. *J Magn Reson*. 2001;148:289–297.
25. Idiyatullin D, Suddarth S, Corum CA, Adriany G, Garwood M. Continuous SWIFT. *J Magn Reson*. 2012;220:26–31.
26. Sohn SM, Vaughan JT, Lagore RL, Garwood M, Idiyatullin D. In vivo MR imaging with simultaneous RF transmission and reception. *Magn Reson Med*. 2016;76:1932–1938.
27. Özen AC, Atalar E, Korvink JG, Bock M. In vivo MRI with concurrent excitation and acquisition using automated active analog cancellation. *Sci Rep*. 2018;8:10631.
28. Liimatainen T, Sorce DJ, O'Connell R, Garwood M, Michaeli S. MRI contrast from relaxation along a fictitious field (RAFF). *Magn Reson Med*. 2010;64:983–994.
29. Pauly J, Nishimura D, Macovski A. A k-space analysis of small-tip-angle excitation. *J Magn Reson (1969)*. 1989;81:43–56.
30. Littin S, Jia F, Layton KJ, et al. Development and implementation of an 84-channel matrix gradient coil. *Magn Reson Med*. 2018;79:1181–1191.
31. Ertan K, Taraghinia S, Sadeghi A, Atalar E. A z-gradient array for simultaneous multi-slice excitation with a single-band RF pulse. *Magn Reson Med*. 2018;80:400–412.

## SUPPORTING INFORMATION

Additional Supporting Information may be found online in the Supporting Information section.

**FIGURE S1** Example multiband adiabatic pulse waveforms. Waveform plot for multiphoton multiband adiabatic inversion pulse generated by KSFoundation Epic's sequence plotting. In this case, The DC gradient is 0.2 G/cm, the AC gradient is 1.5 times the DC gradient strength, and the hyperbolic secant RF pulse has nominal parameters $A_0 = 22$ μT, $\mu = 4.9$, $\beta = 800$ rad/s. The pulse duration is 8 ms. The AC gradient frequency is 2737.5 Hz, which leads to a maximum gradient slew rate of 51.6 T/m/s, which is well within standard hardware capabilities

**FIGURE S2** Example multiband adiabatic pulse simulations. An 8 ms hyperbolic secant RF pulse with parameters $A_0 = 22$ μT, $\mu = 4.9$, $\beta = 800$ rad/s is simulated with (A) only a DC gradient, (B) a DC gradient and a 5475 Hz gradient with 1.5 times the amplitude of the DC, and (C) a DC gradient and a 2737.5 Hz gradient with 1.5 times the amplitude of the DC. One, three, and five adiabatic inversion bands can respectively be seen in the field of view. Red numbers indicate the full width half maximum (FWHM) in kHz. Any slight differences in FWHM may be because of slight asymmetries in the BS shift or numerical error

**TABLE S1** Example Bessel function values. Note that as the ratio of z-axis RF strength to frequency increases, higher order multiphoton effects start to become non-negligible. Also note that multiphoton efficiencies oscillate with the ratio, and the zero crossings of Bessel function are not quite periodic

**VIDEO S1** Two-photon excitation simulation with lower $B_{1,z}$. The magnetization vector nutation path is visualized in 3D for a two-photon excitation in the Larmor frequency rotating frame. The xy-RF frequency is pre-compensated for BS-shift as described in the main text. An ~360° hard pulse is simulated. $\omega_z$ was chosen to be relatively small so that the magnetization vector movement can be easily followed visually. For visualization purposes, the red line representing the magnetization path gets darker in color with decreasing z-position

**VIDEO S2** Two-photon excitation simulation with medium $B_{1,z}$

**VIDEO S3** Two-photon excitation simulation with higher $B_{1,z}$

**VIDEO S4** Two-photon excitation simulation with higher $B_{1,xy}$

**VIDEO S5** Two-photon excitation simulation with below Larmor $\omega_{xy}$

**VIDEO S6** Two-photon excitation simulation with large $\omega_z$

**VIDEO S7** Three-photon excitation simulation. The same as Supporting Information Video S3, except that the xy-RF frequency is set to satisfy a three-photon resonance with the corresponding BS-shift compensation

**How to cite this article:** Han V, Liu C. Multiphoton magnetic resonance in imaging: A classical description and implementation. *Magn Reson Med.* 2020;84:1184–1197. https://doi.org/10.1002/mrm.28186

## APPENDIX

## GENERAL MULTIPHOTON EXCITATION WITH A SINGLE XY-PHOTON

In the phase-modulated rotating frame, we have

$$B_{z,eff} = B_0 - \frac{\omega_{xy}}{\gamma}, \tag{A1}$$

$$B_{x,eff} = B_{1,xy}\cos\left(\frac{\gamma B_{1,z}}{\omega_z}\sin(\omega_z t)\right), \tag{A2}$$

$$B_{y,eff} = B_{1,xy}\sin\left(\frac{\gamma B_{1,z}}{\omega_z}\sin(\omega_z t)\right). \tag{A3}$$

Equations A2 and A3 can be combined to form

$$\begin{aligned} B_{xy,eff} &= B_{1,xy}\cos\left(\frac{\gamma B_{1,z}}{\omega_z}\sin(\omega_z t)\right) + iB_{1,xy}\sin\left(\frac{\gamma B_{1,z}}{\omega_z}\sin(\omega_z t)\right) \\ &= B_{1,xy}e^{i\frac{\gamma B_{1,z}}{\omega_z}\sin(\omega_z t)}. \end{aligned} \tag{A4}$$

With $J_n$ representing the Bessel function of the first kind with integer order $n$, the generating function of the Bessel function of the first kind is

$$e^{\frac{x}{2}\left(z-z^{-1}\right)} = \sum_{n=-\infty}^{\infty} J_n(x)z^n. \tag{A5}$$

Let $z = e^{i\omega_z t}$, then $i\cdot\sin(\omega_z t) = \frac{1}{2}\left(z - z^{-1}\right)$. Equation A4 becomes

$$\begin{aligned} B_{1,xy}e^{i\frac{\gamma B_{1,z}}{\omega_z}\sin(\omega_z t)} &= B_{1,xy}e^{\frac{\gamma B_{1,z}}{2\omega_z}\left(z-z^{-1}\right)} \\ &= B_{1,xy}\sum_{n=-\infty}^{\infty} J_n\left(\frac{\gamma B_{1,z}}{\omega_z}\right)e^{in\omega_z t}. \end{aligned} \tag{A6}$$

This is known as a Jacobi-Anger expansion. From Equations A1 and A6, resonances occur whenever

$$\omega_{xy} = \gamma B_0 + n\omega_z, \tag{A7}$$

and for each $n$, directly from the amplitude in the phase-modulated rotating frame, the effective angular nutation frequency is

$$\omega_{nut} = \gamma B_{1,xy}J_n\left(\frac{\gamma B_{1,z}}{\omega_z}\right). \tag{A8}$$

## MULTIPHOTON EXCITATION WITH ONE $B_{1,xy}$ AND TWO $B_{1,z}$ FIELDS

In this case, $B_z = B_0 + B_{1,z1}\cos(\omega_{z1}t) + B_{1,z2}\cos(\omega_{z2}t)$ with a single $B_{1,xy}$ field. In our phase-modulated rotating frame, the effective fields are

$$B_{z,eff} = B_0 - \frac{\omega_{xy}}{\gamma}, \tag{A9}$$

$$B_{x,eff} = B_{1,xy}\cos\left(\frac{\gamma B_{1,z1}}{\omega_{z1}}\sin(\omega_{z1}t) + \frac{\gamma B_{1,z2}}{\omega_{z2}}\sin(\omega_{z2}t)\right), \tag{A10}$$

$$B_{y,eff} = B_{1,xy}\sin\left(\frac{\gamma B_{1,z1}}{\omega_{z1}}\sin(\omega_{z1}t) + \frac{\gamma B_{1,z2}}{\omega_{z2}}\sin(\omega_{z2}t)\right). \tag{A11}$$

Let $\alpha = \frac{\gamma B_{1,z1}}{\omega_{z1}}$ and $\beta = \frac{\gamma B_{1,z2}}{\omega_{z2}}$, Equations A10 and A11 can be rewritten in complex notation as

$$\begin{aligned} B_{xy,eff} = B_{1,xy}&\cos\left(\alpha\sin(\omega_{z1}t) + \beta\sin(\omega_{z2}t)\right) \\ &+ iB_{1,xy}\sin\left(\alpha\sin(\omega_{z1}t) + \beta\sin(\omega_{z2}t)\right). \end{aligned} \tag{A12}$$

Or equivalently,

$$B_{xy,eff} = B_{1,xy}e^{i\left(\alpha\sin(\omega_{z1}t) + \beta\sin(\omega_{z2}t)\right)} = B_{1,xy}e^{i\alpha\sin(\omega_{z1}t)}e^{i\beta\sin(\omega_{z2}t)}. \tag{A13}$$

Plugging Equation A6 into Equation A13 results in

$$B_{xy,eff} = B_{1,xy} \sum_{n=-\infty}^{\infty} J_n(\alpha)\, e^{in\omega_{z1}t} \sum_{m=-\infty}^{\infty} J_m(\beta)\, e^{im\omega_{z2}t}, \quad \text{(A14)}$$

$$B_{xy,eff} = \sum_{n=-\infty}^{\infty} \sum_{m=-\infty}^{\infty} B_{1,xy} J_n(\alpha) J_m(\beta)\, e^{i\left(n\omega_{z1}t + m\omega_{z2}t\right)}. \quad \text{(A15)}$$

Equation A15 shows that in the phase-modulated rotating frame, xy-RF has angular frequencies of $n\omega_{z1} + m\omega_{z2}$. Therefore, from Equations A9 and A15, resonances occur whenever $\omega_{xy} = \gamma B_0 + n\omega_{z1} + m\omega_{z2}$, and the effective angular nutation frequency for $n$ and $m$ is

$$\omega_{nut} = \gamma B_{1,xy} J_n\left(\frac{\gamma B_{1,z1}}{\omega_{z1}}\right) J_m\left(\frac{\gamma B_{1,z2}}{\omega_{z2}}\right). \quad \text{(A16)}$$

For more than two frequencies along the z-axis, the analysis straightforwardly extends to having more multiplied Bessel functions, one for each new frequency involved.